Received 4 June 2007
Revised 30 January 2008
Accepted 6 February 2008

An artificial compressibility method for buoyancy-driven flow in heterogeneous saturated packed beds

A homogeneous approach

C.J. Visser, A.G. Malan and J.P. Meyer
Department of Mechanical and Aeronautical Engineering, University of Pretoria, Pretoria, South Africa

Abstract

Purpose – The purpose of this paper is to focus on modeling buoyancy driven viscous flow and heat transfer through saturated packed pebble-beds via a set of homogeneous volume-averaged conservation equations in which local thermal disequilibrium is accounted for.

Design/methodology/approach – The local thermal disequilibrium accounted for refers to the solid and liquid phases differing in temperature in a volume-averaged sense, which is modeled by describing each phase with its own governing equation. The partial differential equations are discretized and solved via a vertex-centered edge-based dual-mesh finite volume algorithm. A compact stencil is used for viscous terms, as this offers improved accuracy compared to the standard finite volume formulation. A locally preconditioned artificial compressibility solution strategy is employed to deal with pressure incompressibility, whilst stabilisation is achieved via a scalar-valued artificial dissipation scheme.

Findings – The developed technology is demonstrated via the solution of natural convective flow inside a heated porous axisymmetric cavity. Predicted results were in general within 10 per cent of experimental measurements.

Originality/value – This is the first instance in which both artificial compressibility and artificial dissipation is employed to model flow through saturated porous materials.

Keywords Convection, Flow, Fluid dynamics, Compressible flow, Porous materials

Paper type Research paper

Nomenclature

Roman Symbols

$\mathcal{A}$	= surface (m^2)	k	= thermal conductivity (W/m K)
$\boldsymbol{B}$	= solid-phase matrix drag ($kg/m^2 s^2$)	k_{eff}	= effective thermal conductivity (W/m K)
c_τ	= pseudo-acoustic velocity (m/s)	$\boldsymbol{n}$	= unit vector perpendicular to a domain boundary
$\boldsymbol{C}_{mn}$	= internal edge coefficient (m^2)	p	= static pressure (Pa)
C_p	= specific heat at constant pressure (J/kg K)	r	= radius (m)
d_p	= particle/sphere diameter (m)	t	= time (s)
$\boldsymbol{g}$	= gravitational acceleration (m/s^2)	T	= temperature (K)

The authors would like to thank North-West University and M-Tech Industrial for the financial and technical support in undertaking the work presented here. The authors would like to acknowledge in particular Professor C.G. du Toit and Mr J. van der Merwe.

International Journal of Numerical Methods for Heat & Fluid Flow
Vol. 18 No. 7/8, 2008
pp. 900-918

0961-5539
DOI 10.1108/09615530810899015

$\mathbf{u}$ = velocity vector (m/s)
$\mathcal{V}$ = volume (m^3)
$\boldsymbol{x}$ = spatial position (m)

Greek symbols
α = fluid-solid interface heat transfer coefficient ($W/m^2 K$)
ϵ = thermal radiative emissivity
ε = porosity or void fraction
μ = coefficient of viscosity (kg/m s)
ρ = density (kg/m^3)
τ = viscous stress tensor ($kg/m\,s^2$)

Superscripts
f, s = fluid/solid phase
j = general tensor notation spatial index

Subscripts
b = homogeneous bed property on the edge of the near-wall region
d_p = based on particle diameter
f, s = fluid/solid phase
i, j = general tensor notation spatial index
m, n = discrete node number
w = porous bed bounding wall
∞ = reference condition

Non-dimensional numbers
Nu_{d_p} = Nusselt number $(\alpha d_p / \langle k_f \rangle^f)$
Pr = Prandtl number $(\langle C_p \rangle^f \langle \mu_f \rangle^f / \langle k_f \rangle^f)$
Re_{d_p} = Reynolds number $(\langle \rho_f \rangle^f \varepsilon \, |\langle \boldsymbol{u} \rangle^f| d_p / \langle \mu_f \rangle^f)$

1. Introduction

The importance of accurately modelling single-phase flow through packed pebble beds is ever more increasing with the advent of new generation packed bed nuclear and catalytic reactors as well as modern electronic cooling systems. To date, several modelling approaches exist, of which some significant ones are arguably pore-scale modelling; a continuum approach using the so-called non-Darcy models; and a volume-averaged continuum approach using a so-called generalised model.

Pore-scale modelling (Magnico, 2003; Pan *et al.*, 2001; Morris *et al.*, 1999) is still prohibitively expensive when applied to realistic engineering systems which involve randomly packed pebble beds. Capturing detailed interstitial flow phenomena is however possible with this approach. The extended Darcy law approach (non-Darcy models) is computationally most efficient, but has the significant deficiency of not fully accounting for boundary and inertial effects (Prasad *et al.*, 1992). The volume-averaged model (also known as the generalised model), initiated by Whitaker (1967), attempts at finding a compromise between the accuracy and computational cost limitations of the aforementioned methods. Here, microscopic volume-averaged governing equations are employed in conjunction with empirical relations to account for pore- or micro-scale phenomena.

Owing to the stated inherent advantages, generalised models are finding increased application. Poulikakos and Bejan (1985), Nithiarasu *et al.* (1996) and Nithiarasu *et al.* (1999) modelled buoyancy-driven flow in fluid-saturated non-Darcian porous media. The latter authors also indicated that the model reduces to the Navier-Stokes equations for porosity equal to one, and that it agrees with the generalised model as used by Vafai *et al.* (1985). Kuipers *et al.* (1992) applied the volume averaging technique to modelling gas-fluidized beds through a continuum description of two fluids in suspension. The generalised-type model has also been successfully applied to describe flow and heat transfer in packed bed nuclear reactors (Becker and Laurien, 2003; van Staden *et al.*, 2004; du Toit *et al.*, 2006; Verkerk, 2000).

In the context of employing the generalised model to simulating flow and heat transfer through nuclear reactors, (Becker and Laurien, 2003) pointed out that the

assumption of local thermal equilibrium between the solid phase and working fluid is inadequate, necessitating multiple equations to enforce conservation of energy for the respective phases. This technique is also supported by amongst others Gunn (1978), Gidaspow (1986), Kuipers *et al.* (1992) and du Toit *et al.* (2006). Finally, the majority of models mentioned assume fluid pressure-incompressibility.

Numerical schemes used to solve the generalised set of governing partial differential equations vary significantly. Massarotti *et al.* (2001) applied finite element discretization and a characteristic-based split (CBS) procedure to deal with the fluid incompressibility and stability (Zienkiewicz and Taylor, 2000). When considering finite volume based models, all work to date involves the cell-centered variant, where a pressure correction (projection) method is employed to deal with pressure-velocity coupling (Becker and Laurien, 2003; van Staden *et al.*, 2004). In the context of modelling flow through saturated packed pebble beds, an artificial compressibility vertex-centered finite volume method has not to date featured. This is therefore the first instance in which both artificial compressibility and the chosen stabilisation scheme, viz. artificial dissipation, is employed to model flow through saturated porous materials. Edge-based vertex-centered finite volume discretization is advantageous when applying boundary conditions as well as in terms of computational efficiency and applicability to hybrid-unstructured meshes (Malan, 2002). Furthermore, the artificial compressibility scheme is sought because of its inherent memory efficiency (Malan *et al.*, 2002; Nithiarasu, 2003) and natural suitability to parallel environments, while allowing for the mutual technology transfer with compressible time-marching solvers.

In this paper, a homogeneous generalised-type governing equation is employed to model buoyancy-driven flow in saturated packed pebble beds. Local thermal disequilibrium is allowed for via describing the energy conservation of the fluid and solid phases individually. Spatial discretization is effected with a compact vertex-centered edge-based dual-mesh finite volume algorithm. The fluid phase is considered pressure-incompressible and dealt with numerically through the use of a recently developed locally-generalised-preconditioned artificial compressibility technique (Malan *et al.*, 2002). All material properties are assumed to be fully non-linear functions of temperature. Scalar-valued (JST) artificial dissipation is employed for the purpose of stabilisation. The compact stencil used for the viscous terms is as developed by Crumpton *et al.* (1997) and applied by Malan (2002). The developed modelling technology is validated via application to simulating the SANA benchmark experiment (Niessen and Stöcker, 1997). Predicted temperatures are compared to experimentally determined values for the purpose of validation.

2. Governing equations

In this work, a homogeneous generalised-type governing equation set similar to that of Vafai and Tien (1981) is employed. This involves the use of the volume-averaging technique coupled with semi-empirical formulae, to describe natural convective flow through saturated randomly packed rigid pebble beds. Similar to others (Kuipers *et al.*, 1992; Becker and Laurien, 2003; du Toit *et al.*, 2006), a two-phase system is considered and the following assumptions made:

- On the volume-averaged scale the porous matrix is assumed isotropic.
- Viscous dissipation effects as well as the kinetic energy contribution to the fluid total energy are assumed negligible. This is justified by the low Mach numbers of the flow involved.
- In addition, all fluid material properties excluding specific heat, are variant with respect to temperature.
- Solid material properties, with the exclusion of thermal conductivity, are assumed invariant with respect to both temperature and pressure. The latter is taken as variant with respect to temperature only.
- No chemical reactions occur.
- Heat transfer as a result of fluid dispersion is assumed negligible.

In addition to the above, it is assumed that there is no significant temperature gradient within a specific pebble. This is due to steady-state natural convective flows being considered.

All governing equations are written in terms of intrinsic microscopic volume-averaged quantities. This is defined for a phase γ as follows:

$$\langle \phi_\gamma \rangle^\gamma = \langle \phi_\gamma \rangle^\gamma (t, \mathbf{x}_{\mathcal{V}}) = \frac{1}{\mathcal{V}_\gamma} \int_{\mathcal{V}_\gamma(\mathbf{x})} \phi_\gamma(t, \mathbf{x}) d\mathcal{V} \tag{1}$$

where $\phi_\gamma(t, x \in \mathcal{V}_\gamma)$ denotes a scalar field which describes a property of the phase γ at a time t and spatial position $\mathbf{x}$. Further, $\mathcal{V}_\gamma(\mathbf{x})$ is the volume over which averaging is applied, with geometric center $\mathbf{x}_{\mathcal{V}}$.

The system of governing equations now follows. These are written for a generic rectangular/cylindrical 2D Cartesian coordinate system. The radius corresponding to the cylindrical coordinate system is denoted r. The latter is aligned with the x_1 axis, and to be set as $r = 1$ in the case of a standard 2D rectangular coordinate system.

Mass conservation of the fluid phase:

$$\frac{\partial (r \langle \rho_f \rangle^f)}{\partial t} + \frac{\partial}{\partial x_j} (r \langle \rho_f \rangle^f \langle u_j \rangle^f) = 0 \tag{2}$$

where $\langle \rho_f \rangle^f$ is the intrinsic microscopic volume-averaged density of the fluid, $\langle u_j \rangle^f$ is the intrinsic velocity component of the fluid in Cartesian coordinate direction x_j. Momentum conservation of the fluid phase reads:

$$\begin{aligned} &\frac{\partial (r \langle \rho_f \rangle^f \langle u_i \rangle^f)}{\partial t} + \frac{\partial}{\partial x_j} (r \langle \rho_f \rangle^f \langle u_j \rangle^f \langle u_i \rangle^f) + r \frac{\partial \langle p \rangle^f}{\partial x_i} \\ &- \frac{\partial}{\partial x_j} (r \langle \tau_{ij} \rangle^f) - r \langle \rho_f \rangle^f \langle g_i \rangle^f - \frac{r}{\varepsilon} B_i + \delta_{1i} (1 - \delta_{is}) \langle \tau_{33} \rangle^f = 0 \end{aligned} \tag{3}$$

where $\langle p \rangle^f$ denotes the intrinsically averaged fluid static pressure, $\langle \tau_{ij} \rangle^f$ is the microscopic volume-averaged viscous stress term, $\langle g_i \rangle^f$ is the body force in direction x_i and B_i is the drag due to the solid matrix. The buoyancy force due to gravity is accounted for via density being taken as an explicit function of temperature. Note that

for a two dimensional cylindrical coordinate system $\zeta = 0$. Furthermore, application of the governing equation set to a rectangular coordinate system requires $\zeta = 1$. Finally, ε denotes porosity and is calculated as:

$$\varepsilon = \varepsilon(\mathbf{x}_{\mathcal{V}}) = \frac{1}{\mathcal{V}} \int_{\mathcal{V}_f(\mathbf{x})} d\mathcal{V} \tag{4}$$

where $\mathcal{V}$ is the spatial volume over which volume-averaging is applied. Finally, the axi-symmetric stress term $\langle \tau_{33} \rangle^f$ is calculated as:

$$\langle \tau_{33} \rangle^f = -\frac{2}{3} \langle \mu_f \rangle^f \left(\frac{1}{r} \frac{\partial}{\partial x_1} (r \langle u_1 \rangle^f) + \frac{\partial \langle u_2 \rangle^f}{\partial x_2} \right) + 2 \langle \mu_f \rangle^f \left(\frac{\langle u_1 \rangle^f}{r} \right) \tag{5}$$

where $\langle \mu_f \rangle^f$ is the intrinsic fluid phase dynamic viscosity.

The energy conservation equation for the fluid phase reads:

$$\begin{aligned} &\frac{\partial \left(r \langle \rho_f \rangle^f \langle C_{p_f} \rangle^f \langle T_f \rangle^f \right)}{\partial t} + \frac{\partial}{\partial x_j} \left(r \langle \rho_f \rangle^f \langle C_{p_f} \rangle^f \langle T_f \rangle^f \langle u_j \rangle^f \right) \\ &\quad - \frac{\partial}{\partial x_j} \left(r \langle k_f \rangle^f \frac{\partial \langle T_f \rangle^f}{\partial x_j} \right) + \frac{6(1-\varepsilon)}{\varepsilon d_p} r \alpha \left(\langle T_f \rangle^f - \langle T_s \rangle^s \right) = 0 \end{aligned} \tag{6}$$

where $\langle C_{p_f} \rangle^f$, $\langle k_f \rangle^f$ and $\langle T_f \rangle^f$ are, respectively, the intrinsic specific heat, thermal conductivity and temperature of the fluid. Further, α is the heat transfer coefficient between the fluid and solid (pebble), $\langle T_s \rangle^s$ is the average pebble temperature and d_p is the pebble diameter.

The energy conservation of the solid phase reads:

$$\frac{\partial}{\partial t} \left(r \langle \rho_s \rangle^s \langle C_{p_s} \rangle^s \langle T_s \rangle^s \right) - \frac{\partial}{\partial x_j} \left(\frac{r k_{eff}}{(1-\varepsilon)} \frac{\partial \langle T_s \rangle^s}{\partial x_j} \right) + \frac{6}{d_p} r \alpha \left(\langle T_s \rangle^s - \langle T_f \rangle^f \right) = 0 \tag{7}$$

where $\langle C_{p_s} \rangle^s$, $\langle \rho_s \rangle^s$ and k_{eff} are, respectively, the solid-phase intrinsic specific heat, density and superficial effective thermal conductivity between the pebbles. Note that α and $\langle T_s \rangle^s$ are as defined for the fluid-phase energy conservation equation.

2.1 Constitutive equations

As noted previously, in this work the pore scale or microscopic phenomena are accounted for via volume-averaged constitutive equations. These are the solid matrix drag $\mathbf{B}$, fluid-solid interface heat transfer coefficient α and effective thermal conductivity k_{eff}. The solid matrix drag is approximated using the vectorial form of the Ergun (1952) relation as proposed by Radestock and Jeschar (1971):

$$B_i = -\left(150 \frac{(1-\varepsilon)^2}{\varepsilon} \frac{\langle \mu_f \rangle^f}{d_p^2} + 1.75(1-\varepsilon) \frac{\langle \rho_f \rangle^f}{d_p} |\langle \mathbf{u} \rangle^f| \right) \langle u_i \rangle^f \tag{8}$$

where $\langle \mu_f \rangle^f$ is the fluid dynamic viscosity and $|\langle \mathbf{u} \rangle^f|$ the local fluid velocity norm.

The volumetric heat transfer coefficient between the fluid and solid phases (denoted α) in equations (6) and (7) is taken from the correlation of Gunn (1978):

$$Nu_{d_p} = (7 - 10\varepsilon + 5\varepsilon^2)(1 + 0.7\,Re_{d_p}^{0.2}\,Pr^{1/3}) + (1.33 - 2.4\varepsilon + 1.2\varepsilon^2)\,Re_{d_p}^{0.7}\,Pr^{1/3} \quad (9)$$

where Nu_{d_p}, Re_{d_p} and Pr are, respectively, the Nusselt-, local Reynolds- and Prandtl numbers. These are defined as:

$$Nu_{d_p} = \frac{\alpha d_p}{\langle k_f \rangle^f}, \quad Pr = \frac{\langle C_{p_f} \rangle^f \langle \mu_f \rangle^f}{\langle k_f \rangle^f}, \quad Re_{d_p} = \frac{\langle \rho_f \rangle^f d_p \varepsilon |\langle \mathbf{u} \rangle^f|}{\langle \mu_f \rangle^f} \quad (10)$$

Finally, the effective thermal conductivity (denoted k_{eff}) in equation (7) is calculated based on the model by Zehner and Schlünder (1970) in the form proposed by the International Atomic Energy Agency – IAEA (2001). It is calculated as:

$$k_{eff} = k_{eff}^{sc} + k_{eff}^{sr} + k_{eff}^{sf} \quad (11)$$

where the respective simultaneous modes of heat transfer accounted for are: heat transfer due to solid-phase conduction and conduction across the contact interfaces between pebbles (k_{eff}^{sc}); radiative heat transfer between and conduction through the pebbles (k_{eff}^{sr}); and finally k_{eff}^{sf} accounts for conduction through the pebble solid material as well as the stationary gas component filling the interstitial voids.

2.2 Boundary conditions

Both Dirichlet- and Neumann-type boundary conditions are applied to the domain boundaries (a detailed schematic diagram follows in Section 4). The former includes fluid no-slip conditions as well as prescribed temperatures for the fluid and solid phases. The Neumann conditions include adiabatic and constant heat flux. In the case of the latter, the fluid temperature is assumed representative of the actual wall temperature[1] and the heat influx to the solid phase then prescribed with a radiative-type boundary condition from the model of Schlünder, as documented by Fundamenski and Gierszewski (1991, 1992):

$$q_{solid} = -k_{eff} \frac{\partial \langle T_s \rangle^s}{\partial x_i} n_i = h_r \left((\langle T_f \rangle^f)^4 - (\langle T_b \rangle^s)^4 \right) \quad (12)$$

with:

$$h_r = \sigma \left[\frac{1}{\epsilon_s} + \frac{1}{\epsilon_w} - 1 \right]^{-1} \quad (13)$$

where σ denotes the Stefan-Boltzmann constant ($\simeq 5.67 \times 10^{-8}\,\mathrm{W/m^2\,K^4}$), ϵ_s and ϵ_w are the emissivity of the solid phase and wall, respectively, and $\langle T_b \rangle^s$ denotes the solid-phase temperature on the edge of the near-wall region. The latter is defined as the region extending from the wall to one sphere radius into the bed. Further, $\langle T_b \rangle^s$ is calculated by extrapolating linearly from the wall to a distance of half a sphere diameter into the bed, perpendicular to the wall as:

$$\langle T_b \rangle^s \approx \left(\left. \frac{\partial \langle T_s \rangle^s}{\partial x_i} \right|_w n_i \right) \left(-\frac{d_p}{2} \right) + \langle T_s \rangle^s |_w \quad (14)$$

where the subscript w indicates property values at the wall and $\mathbf{n}$ is the outward-pointing unit vector normal to the wall.

In completing the constant heat flux boundary condition, the fluid-phase heat flux is now prescribed as:

$$-\varepsilon\langle k_f\rangle^f \frac{\partial\langle T_f\rangle^f}{\partial x_i} n_i = q_{\text{input}} - q_{\text{solid}} \tag{15}$$

where q_{input} is the specified heat input to the physical setup and q_{solid} is the heat flux as calculated in equation (12).

3. Solution procedure

In describing the solution procedure, it is instructive to write the system of governing equations in the following form:

$$\frac{\partial \mathbf{W}}{\partial t} + \frac{\partial \mathbf{F}^j}{\partial x_j} + r\frac{\partial \mathbf{H}}{\partial x_j} - \frac{\partial \mathbf{G}^j}{\partial x_j} = \mathbf{S} \tag{16}$$

where:

$$\mathbf{W} = \begin{pmatrix} r\langle\rho_f\rangle^f \\ r\langle\rho_f\rangle^f\langle u_1\rangle^f \\ r\langle\rho_f\rangle^f\langle u_2\rangle^f \\ r\langle\rho_f\rangle^f\langle C_{p_f}\rangle^f\langle T_f\rangle^f \\ r\langle\rho_s\rangle^s\langle C_{p_s}\rangle^s\langle T_s\rangle^s \end{pmatrix}, \quad \mathbf{F}^j = \begin{pmatrix} r\langle\rho_f\rangle^f\langle u_j\rangle^f \\ r\langle\rho_f\rangle^f\langle u_1\rangle^f\langle u_j\rangle^f \\ r\langle\rho_f\rangle^f\langle u_2\rangle^f\langle u_j\rangle^f \\ r\langle\rho_f\rangle^f\langle C_{p_f}\rangle^f\langle T_f\rangle^f\langle u_j\rangle^f \\ 0 \end{pmatrix}$$

$$\mathbf{H} = \begin{pmatrix} 0 \\ \langle p\rangle^f\delta_{1j} \\ \langle p\rangle^f\delta_{2j} \\ 0 \\ 0 \end{pmatrix}, \quad \mathbf{G}^j = \begin{pmatrix} 0 \\ r\langle\tau_{1j}\rangle^f \\ r\langle\tau_{2j}\rangle^f \\ r\langle k_f\rangle^f \frac{\partial\langle T_f\rangle^f}{\partial x_j} \\ \frac{\mathrm{rk}_{eff}}{(1-\varepsilon)} \frac{\partial\langle T_s\rangle^s}{\partial x_j} \end{pmatrix}$$

$$\mathbf{S} = \begin{pmatrix} 0 \\ r\langle\rho_f\rangle^f\langle g_1\rangle^f + \frac{r}{\varepsilon}B_1 - (1-\delta_{1\zeta})\langle\tau_{33}\rangle^f \\ r\langle\rho_f\rangle^f\langle g_2\rangle^f + \frac{r}{\epsilon}B_2 \\ -\frac{6(1-\varepsilon)}{\varepsilon d_p}r\alpha\left(\langle T_f\rangle^f - \langle T_s\rangle^s\right) \\ -\frac{6}{d_p}r\alpha\left(\langle T_s\rangle^s - \langle T_f\rangle^f\right) \end{pmatrix} \tag{17}$$

where the nomenclature is as defined previously.

3.1 Spatial discretization

Spatial discretization commences by casting the governing equations into weak form, followed by the transformation of volume integrals into surface integrals via the application of the divergence theorem:

$$\int_{\mathcal{V}_\xi}\frac{\partial\mathbf{W}}{\partial t}d\mathcal{V} + \int_{\mathcal{A}_\xi}\mathbf{F}^j n^j d\mathcal{A} + \bar{r}\int_{\mathcal{A}_\xi}\mathbf{H}^j n^j d\mathcal{A} - \int_{\mathcal{A}_\xi}\mathbf{G}^j n^j d\mathcal{A} = \bar{\mathbf{S}}_\xi \tag{18}$$

Here, $\mathcal{A}_\xi$ is the surface bounding $\mathcal{V}_\xi$ and $\mathbf{n}$ is the outward-pointing unit vector in the direction normal to the boundary segment $d\mathcal{A}$. Further, $\bar{r}$ and $\bar{\mathbf{S}}_\xi$, respectively, denote the spatially averaged radius and source terms, where averaging is done with respect to $\mathcal{V}_\xi$.

The volumes or sub-domains over which are integrated are constructed on the mesh as per Vahdati *et al.* (1989) (similar to Sørensen *et al.* (2002)). In two dimensions, this involves connecting edge midpoints and element centroids such that only one node is present in each control volume. This is shown schematically for a node m in Figure 1. A volume (sub-domain) associated with a node m for instance, is designated $\mathcal{V}_m$ and the bounding surface by $\mathcal{A}_m$.

The discrete form of a typical surface integral in equation (18), computed for the volume surrounding a node m, reads:

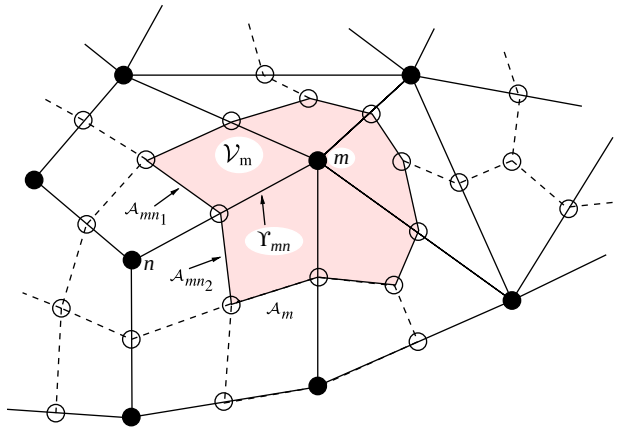

Note: Here Υ_{mn} depicts the edge connecting nodes m and n

Figure 1.
Schematic diagram of the construction of the median-dual-mesh on hybrid grids

$$\int_{\mathcal{A}_m} \mathbf{G}^j n^j d\mathcal{A} \approx \sum_{\Upsilon_{mn} \cap \mathcal{V}_m} \overline{\mathbf{G}^j_{mn}} C^j_{mn} \tag{19}$$

where $\overline{\mathbf{G}^j}$ is the flux value calculated at the edge centre and Υ_{mn} denotes all edges connected to node m. The bounding surface information is stored in an edge-wise manner. These are termed edge-coefficients (denoted C^j_{mn} in equation (19)) and in the case of internal edges are defined as:

$$\mathbf{C}_{mn} = \mathbf{n}^{mn_1} \mathcal{A}_{mn_1} + \mathbf{n}^{mn_2} \mathcal{A}_{mn_2} \tag{20}$$

where m and n denote the attached nodes and $\mathcal{A}_{mn_1}$ is a bounding surface-segment intersecting the edge. Storing information in an edge-wise manner is advantageous in that one loop over edges computes all edge contributions whereas element-based methods require the computation of each edge contribution at least twice (Luo *et al.*, 1994).

It is expected that buoyancy-driven flow through densely packed beds contains regions which are highly diffusive on a volume-averaged level. The diffusive spatial terms (second-order spatial derivatives) are therefore to be discretized in an accurate manner, which does not suffer from odd-even decoupling. To this end, the edge-based compact stencil algorithm developed by Crumpton *et al.* (1997) is employed and as described by Lewis and Malan (2005).

3.2 Artificial compressibility

Having spatially discretized the set of governing equations, the following semi-discrete expression results at a node m:

$$\left.\frac{\partial \mathbf{W}}{\partial t}\right|_m = \mathbf{RHS}_m \tag{21}$$

where **RHS** denotes the discretized spatial terms placed on the right-hand side. The above expression is not solvable as fluid incompressibility yields it overly stiff. This is addressed by employing the method of artificial compressibility (AC), and in a consistent manner (Malan *et al.* (2002)) as follows:

$$\frac{\partial \mathbf{W}}{\partial \mathbf{Q}} \left.\frac{\partial \mathbf{Q}}{\partial t}\right|_m = \mathbf{RHS}_m \tag{22}$$

where:

$$\frac{\partial \mathbf{W}}{\partial \mathbf{Q}} = \begin{pmatrix} r\frac{\partial \langle \rho_f \rangle^f}{\partial \langle p \rangle^f} & 0 & 0 & 0 & 0 \\ r\langle u_1 \rangle^f \frac{\partial \langle \rho_f \rangle^f}{\partial \langle p \rangle^f} & r\langle \rho_f \rangle^f & 0 & 0 & 0 \\ r\langle u_2 \rangle^f \frac{\partial \langle \rho_f \rangle^f}{\partial \langle p \rangle^f} & 0 & r\langle \rho_f \rangle^f & 0 & 0 \\ r\langle C_{p_f} \rangle^f \langle T_f \rangle^f \frac{\partial \langle \rho_f \rangle^f}{\partial \langle p \rangle^f} & 0 & 0 & r\langle \rho_f \rangle^f \langle C_p \rangle^f & 0 \\ 0 & 0 & 0 & 0 & r\langle \rho_s \rangle^s \langle C_{p_s} \rangle^s \end{pmatrix} \tag{23}$$

and:

$$\mathbf{Q} = \begin{pmatrix} \langle p \rangle^f \\ \langle u_1 \rangle^f \\ \langle u_2 \rangle^f \\ \langle T_f \rangle^f \\ \langle T_s \rangle^s \end{pmatrix} \tag{24}$$

Artificial compressibility is introduced by replacing the term $\partial \langle \rho_f \rangle^f / \partial \langle p \rangle^f$, which is equal to $1/c^2$ for compressible flow (where c is the acoustic velocity), with a pseudo-acoustic velocity approximation $1/c_\tau^2$. Here, c_r is designated the free AC parameter which is to be calculated in an appropriate manner. Since the acoustic velocity is altered, the time accuracy is destroyed and time t replaced with pseudo-time t_r. Following Malan *et al.* (2002), a locally generalised preconditioned system results by defining the Jacobian term as follows:

$$\left.\frac{\partial \mathbf{W}}{\partial \mathbf{Q}}\right|_\tau = \begin{pmatrix} \frac{r}{c_\tau} & 0 & 0 & 0 & 0 \\ a_u \frac{r\langle u_1 \rangle^f}{c_\tau^2} & r\langle \rho_f \rangle^f & 0 & 0 & 0 \\ a_u \frac{r\langle u_2 \rangle^f}{c_\tau^2} & 0 & r\langle \rho_f \rangle^f & 0 & 0 \\ a_T \frac{r\langle C_{p_f} \rangle^f \langle T_f \rangle^f}{c_\tau^2} & 0 & 0 & r\langle \rho_f \rangle^f \langle C_{pf} \rangle^f & 0 \\ 0 & 0 & 0 & 0 & r\langle \rho_s \rangle^s \langle C_{p_s} \rangle^s \end{pmatrix} \tag{25}$$

where c_r and a_u are calculated similar to Malan *et al.* (2002) and:

$$a_T = \begin{cases} 0 & \text{if} \quad a_u = 0 \\ 1 & \text{if} \quad a_u > 0 \end{cases} \tag{26}$$

The above relation affects preconditioning of the fluid energy equation.

3.3 Stabilisation

The spatial discretization method outlined in Section (3.1) may result in non-physical spurious oscillations due to the presence of convective terms. Stabilizing the convective terms without loosing accuracy is done using the scalar-valued artificial dissipation (JST) model as developed by Jameson *et al.* (1981). This involves adding an additional artificial dissipation term to the semi-discrete system of equations (equation (22)), resulting in the following expression for a node m:

$$\left.\frac{\partial \mathbf{W}}{\partial \mathbf{Q}} \frac{\partial \mathbf{Q}}{\partial t}\right|_m = \mathbf{RHS}_m + \mathbf{D}_m \tag{27}$$

where $\mathbf{D}_m$ denotes the stabilizing term. The dissipation term is constructed through the use of a biharmonic operator as per Mavriplis (1990):

$$\mathbf{D}_m = -\Psi_4 \frac{\lambda_m + \lambda_n}{2} \sum_{\Upsilon_{mn} \cap \Upsilon_m} (\nabla^2 \Theta_n - \nabla^2 \Theta_m) \tag{28}$$

where Ψ_4 is an empirical constant and λ_m is an isotropic scaling coefficient at node m which is calculated as:

$$\lambda_m = \sum_{\Upsilon_{mn} \cap \Upsilon_m} |\mathbf{u} \cdot \mathbf{C}_{mn}| + c_\tau |\mathbf{C}_{mn}| \tag{29}$$

The Laplacian $\nabla^2 \Theta_m$ in equation (28) is approximated in a manner which is consistent with the method employed for preconditioning (Malan *et al.*, 2002):

$$\nabla^2 \Theta_m = \sum_{\Upsilon_{mn} \cap \Upsilon_m} \overline{\frac{\partial \mathbf{W}}{\partial \mathbf{Q}}}\Big|_{mn} (\mathbf{Q}_n - \mathbf{Q}_m) \tag{30}$$

where $\overline{\partial \mathbf{W}}/\overline{\partial \mathbf{Q}}|_{mn}$ is the edge averaged Jacobian term. Note that the vector $\mathbf{Q}$ in the above equation denotes the incompressible flow dependent variable (equation (24)).

3.4 Temporal discretisation and solution procedure

The pseudo-temporal terms are discretized using an explicit single-stage time-marching method. A multistage Runge-Kutta time-stepping scheme initially implemented, was found to result in no computational advantage. This is as the latter was found to be advantageous when applied to convection-dominated flows, whereas the flow considered in this work is predominantly diffusive in nature.

4. Numerical tests

The developed numerical technology is validated by application to a benchmark problem viz. the SANA test setup at the Jülich Research Center (Niessen and Stöcker, 1997). The setup, which is shown schematically in Figure 2, consists of a cylindrical vessel which is 1 m in height with inner and outer radii of 0.071 and 0.75 m, respectively. The vessel is filled with 60 mm randomly packed graphite pebbles and filled with either helium[2] or nitrogen and pressurised to 1 bar. The heat input to the system is via a centrally placed electrical heater, spanning various fractions of the total height. The following two test conditions were selected for the purpose of validating the accuracy of the developed modelling technology:

(1) Steady state test with heating element spanning the full length of the pebble bed and helium as the working fluid. The selected nominal heating power input is 5 kW.

(2) Similar operating conditions to the aforementioned, with the exception of a heating power input increase to 35 kW.

Note that the above two test cases were selected, as these represent the two extremes in terms of total heat input. Further note that mesh independent solutions (to within 2 per cent) are quoted in all cases[3].

The heat transfer processes to be modelled are the influx of heat from the inner wall to both the working fluid and solid pebbles, conduction and radiative heat transfer

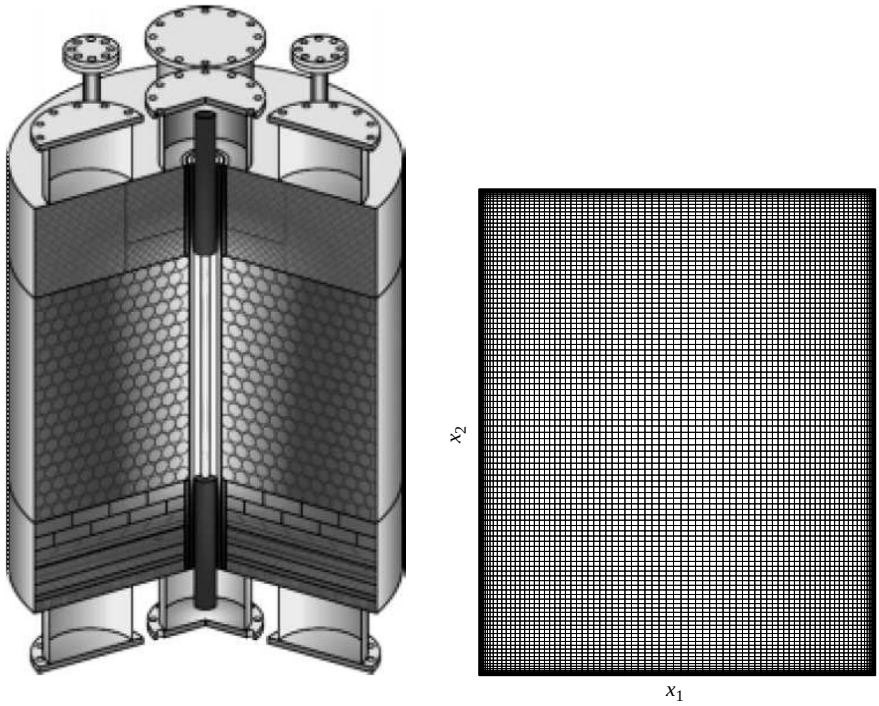

Figure 2.
Schematic diagram of the SANA test-setup (left) with central heating element (Niessen and Stöcker, 1997), and the representative axi-symmetric mesh used (right)

within the solid phase, convective heat transfer between the solid and fluid phase whilst conduction and convective heat transfer are the modes of heat transfer within the fluid phase. The top and bottom walls are insulated and therefore treated as adiabatic.

The above was described by solution of the stated governing equations on a two-dimensional axi-symmetric domain to which the following boundary conditions were applied (Figure 3):

- No-slip boundary conditions are applied to all the walls.
- The top and bottom walls are treated as adiabatic.
- A constant uniform heat flux is applied to the inner wall (5 kW: 9.7976×10^3 W/m^2, 35 kW: 7.22857×10^4 W/m^2).
- A constant temperature field is applied to the outer wall. For this purpose, temperatures applied are taken from the experimental measurements (Niessen and Stöcker, 1997) (5 kW: $T_\infty(x_2) = -50.6x_2^2 + 64.0x_2 + 338.8$ (K), $T_\infty(x_2) = -187.4x_2^2 + 205.7x_2 + 520.2$(K)).

The temperature-dependent material properties for helium are as prescribed by the Nuclear Safety Standards Commission (KTA, 1978), while the material properties for graphite are from the IAEA (2001) and Niessen and Stöcker (1997). The mesh for both the 5 and 35 kW test cases is shown in Figure 2 (right). It contains 9,296 elements with local refinement near the walls to capture the larger velocity gradients expected in these regions as a result of the no-slip boundary condition employed. Note that in this work it is not expected that wall-channeling effects will be accurately modelled due to

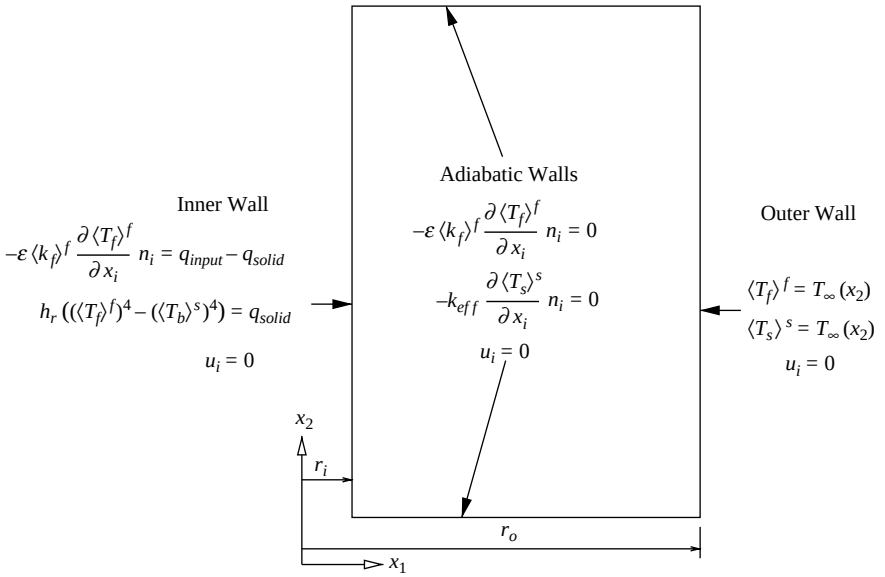

Figure 3.
Schematic diagram of the geometry and boundary conditions applied

Note: Here r_i and r_o denote, respectively, the internal and external radius and q the specified heat influx(W/m^2)

the simplifying assumption of homogeneous porosity. The proper modelling of these is noted for further work via a fully heterogeneous model.

The calculated velocities at a section through the vertical centreline of the vessel are shown in Figure 4. Note that although the authors are not aware of any definitive numerical or experimental data with which to compare the calculated velocities, the spatial discretization error was eliminated via mesh independence. The velocity peak of the 35 kW case is substantially lower and less sharp than that of the 5 kW test. This is attributed to the increase in viscosity of the helium at the elevated

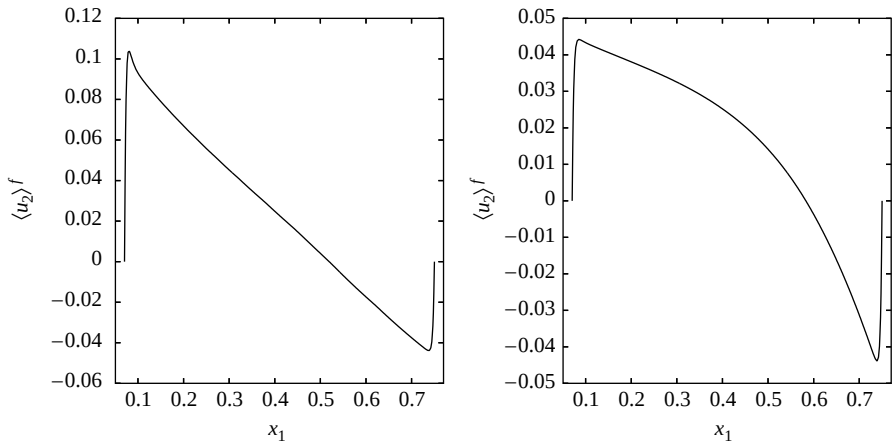

Figure 4.
Calculated vertical velocities in radial section at 0.5 m vertical elevation, for 5 kW (left) and 35 kW (right)

temperatures. The velocity distributions are non-symmetrical as a result of the axi-symmetric geometry as well as the temperature dependence of the material properties. Figure 5 shows the natural convection currents present inside the vessel, with the streamlines indicating the direction of the velocity vectors.

The predicted pebble temperature distribution at three different heights are compared to measurements in Figure 6. The calculated values are seen to compare reasonably well with experimental data. Agreement between the slope of the predicted temperature distribution and experimental data indicates that the effective thermal conductivity is calculated to within acceptable limits. Note the large difference in temperature reach for the respective cases, which explains the large difference in fluid properties leading to the counter-intuitive velocity distributions noted in Figure 4.

Figure 7 shows the large deviations between the predicted solid and fluid temperatures that occur close to the hot inner wall. This is due to local thermal disequilibrium being allowed for. The predicted fluid and solid temperatures in the central region of the pebble bed are however almost identical (this is more so for the 5 kW case). A similar observation to the aforementioned was made by Becker and Laurien (2003) for the steady 35 kW helium test case, where a maximum deviation of less than 10 K was recorded between the solid and fluid phases at spatial locations removed from the near-wall region.

In Figure 8, the deviation between the predicted and measured solid-phase temperatures, presented as a normalized temperature deviation, is shown. The aforementioned is calculated as follows:

$$\Delta\langle T_s\rangle^s_{\text{normalized}} = \frac{\left|\langle T_s\rangle^s_{\text{predicted}} - \langle T_s\rangle^s_{\text{measured}}\right|}{\langle T_s\rangle^s_{\max} - \langle T_s\rangle^s_{\min}} \tag{31}$$

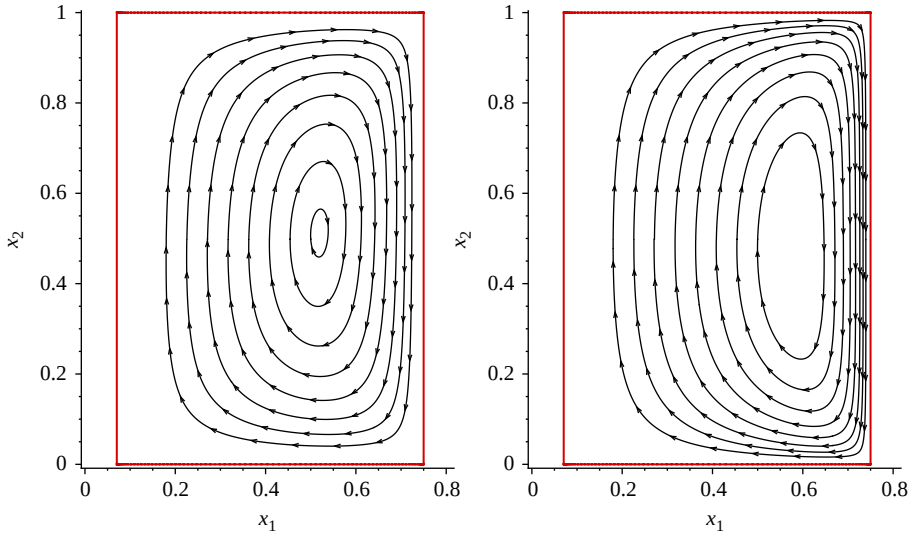

Figure 5.
Flow streamlines for the 5 kW (left) and 35 kW (right) cases

where $\langle T_s \rangle^s_{\max}$ and $\langle T_s \rangle^s_{\min}$ are, respectively, the maximum and minimum temperatures measured in the bed. The maximum normalized disparity between the predicted and measured data is seen to be 0.18, which is located close to the inner wall. It is hoped that this may be improved upon in future work by properly accounting for porosity variation in the near-wall region (via a heterogeneous model). Finally, the average normalized temperature difference (calculated using all data points), are 0.035 and 0.032 for the 5 and 35 kW cases, respectively. This corresponds to a 3.5 and 3.2 per cent average deviation, which is considered to be commendable.

The average residual plots for the respective test cases are shown in Figure 9, where the residual is calculated as the Euclidean norm of the **RHS** in equation (22). The six orders of magnitude monotone drop in residual is an indication that the developed modelling technology is sound with regards to convergence and stability.

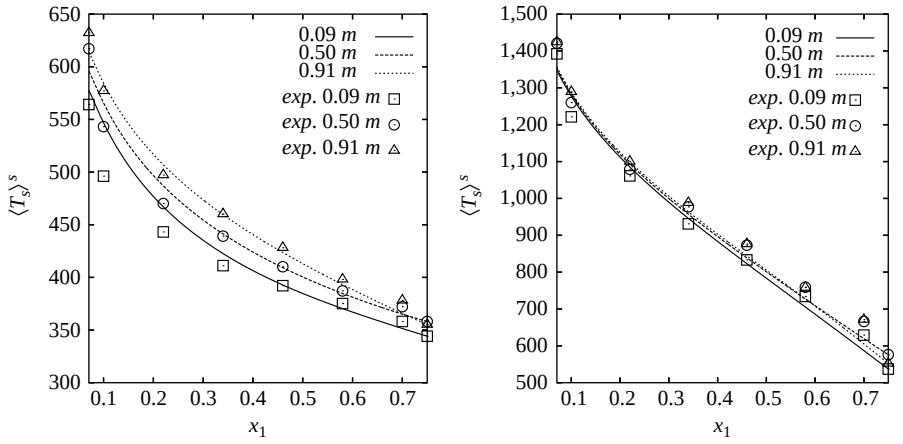

Figure 6.
Predicted pebble temperature distribution compared to experimental (exp.) measurements for 5 kW (left) and 35 kW (right)

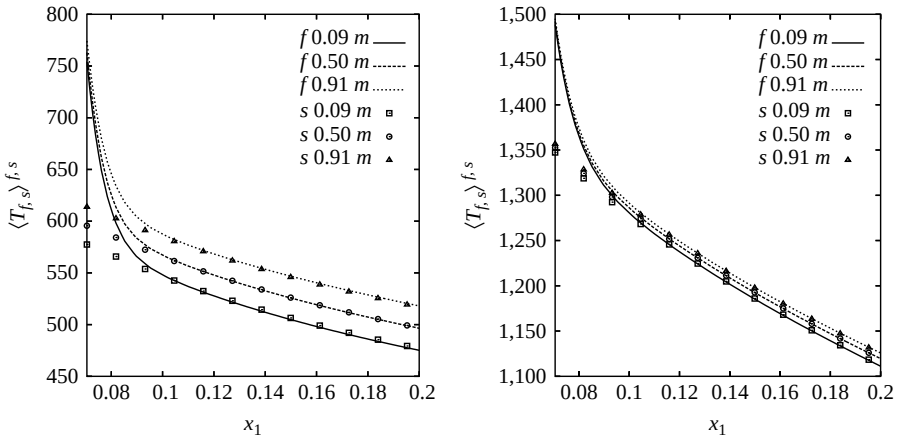

Figure 7.
Comparing predicted temperature distribution of the solid (s) and fluid (f) phases at the inner wall for the 5 kW (left) and 35 kW (right) cases

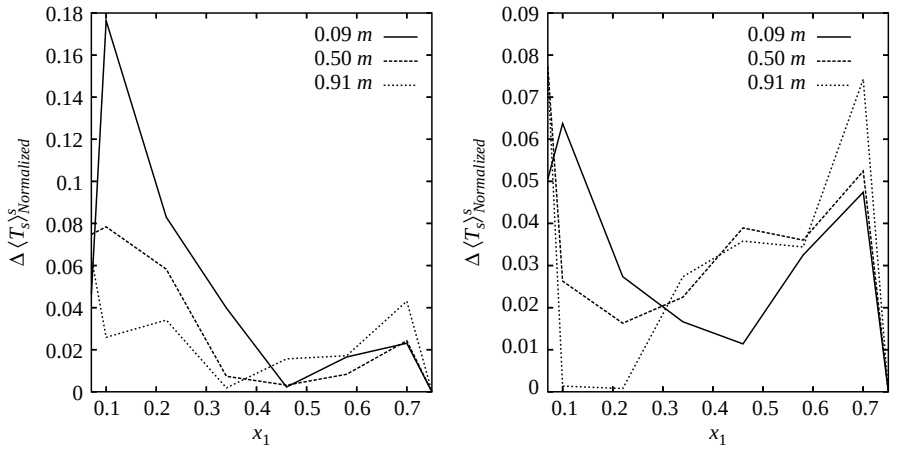

Figure 8.
Normalized temperature disparity of the predicted vs measured solid phase temperatures for the 5 kW (left) and 35 kW (right) cases

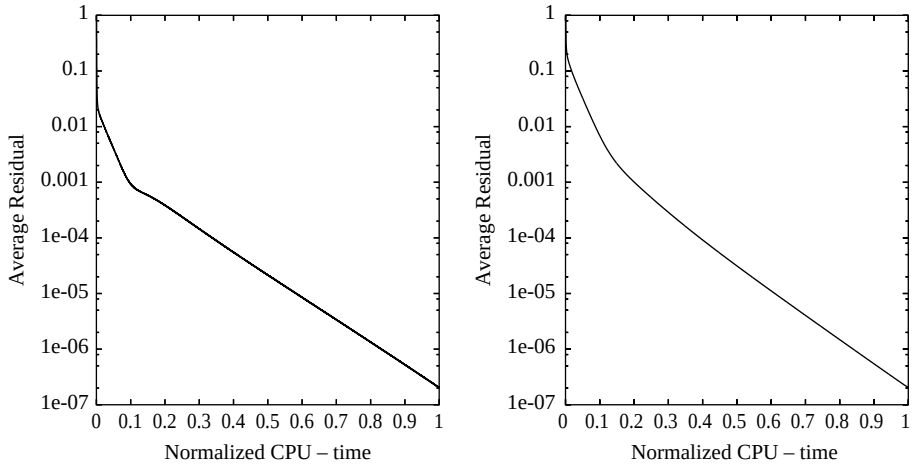

Figure 9.
Average residual for 5 kW (left) and 35 kW (right)

5. Conclusion

This paper detailed modelling buoyancy-driven flow through saturated packed pebble beds. A generalised volume-averaged partial differential governing equation set was employed, and such that local thermal disequilibrium between fluid and solid phases was allowed for. A homogeneous porosity distribution was assumed and material properties taken as fully non-linear with respect to temperature. A compact vertex-centered finite volume spatial discretization scheme was employed and fluid incompressibility dealt with via an artificial compressibility method. The modelling technology was validated by application to modelling a benchmark experiment viz. the SANA test setup. Comparing the simulated- and experimental data indicated an acceptable correlation, with the maximum and average normalized deviations being 0.18 and 0.035, respectively. The aforementioned is located close to a near-wall region,

where porosity variation is dramatic. Future work is recommended to obtain more accurate solutions here via the use of a fully heterogeneous model.

Notes

1. The fluid-wall temperature equivalence is an approximation in this work due to the constant porosity assumption.
2. The pebbles, packing arrangement and stated working fluid are identical to that found in high temperature gas-cooled nuclear reactors, making the chosen test an important benchmark problem in this context.
3. The quoted percentage refers to the deviation of the dependent variables when doubling the mesh size.

References

Becker, S. and Laurien, E. (2003), "Three-dimensional numerical simulation of flow and heat transport in high-temperature nuclear reactors", *Nuclear Engineering and Design*, Vol. 222, pp. 189-201.

Crumpton, P.I., Moinier, P. and Giles, M.B. (1997), "An unstructured algorithm for high Reynolds number flows on highly stretched meshes", in Taylor, C. and Cross, J.T. (Eds), *Numerical Methods in Laminar and Turbulent Flow*, Pineridge Press, Swansea, pp. 561-72.

du Toit, C.G., Rousseau, P.G., Greyvenstein, G.P. and Landman, W.A. (2006), "A systems CFD model of a packed bed high temperature gas-cooled nuclear reactor", *International Journal of Thermal Sciences*, Vol. 45, pp. 70-85.

Ergun, S. (1952), "Fluid flow through packed columns", *Chemical Engineering Progress*, Vol. 48 No. 2, pp. 89-94.

Fundamenski, W.R. and Gierszewski, P.J. (1991), "Comparison of correlations for heat transfer in sphere-pac beds", Canadian Fusion Fuels Technology Project, CFFTP G-9181, pp. 1-42.

Fundamenski, W.R. and Gierszewski, P.J. (1992), "Heat transfer correlations for packed beds", *Fusion Technology*, Vol. 21, pp. 2123-7.

Gidaspow, D. (1986), "Hydrodynamics of fluidization and heat transfer: supercomputer modeling", *ASME Applied Mechanics Reviews*, Vol. 39 No. 1, pp. 1-23.

Gunn, D.J. (1978), "Transfer of heat or mass to particles in fixed and fluidised beds", *International Journal for Heat and Mass Transfer*, Vol. 21, pp. 467-76.

IAEA (2001), "Heat transport and afterheat removal for gas-cooled reactors under accident conditions", Technical Report IAEA-TECDOC-1163, International Atomic Energy Agency, Vienna.

Jameson, A., Schmidt, W. and Turkel, E. (1981), "Numerical simulation of the Euler equations by finite volume methods using Runge-Kutta timestepping schemes", AIAA paper 81-1259, paper presented at AIAA 5th Computational Fluid Dynamics Conference.

KTA (1978), "Reactor core design of high-temperature gas-cooled reactors. Part 1: calculation of the material properties of helium", Technical Report KTA3102.1, Nuclear Safety Standards Commission.

Kuipers, J.A.M., van Duin, K.J., van Beckum, F.P.H. and van Swaaij, W.P.M. (1992), "A numerical model of gas-fluidised beds", *Chemical Engineering Science*, Vol. 47 No. 8, pp. 1913-24.

Lewis, R.W. and Malan, A.G. (2005), "Continuum thermodynamic modeling of drying capillary particulate materials via an edge-based algorithm", *Computer Methods in Applied Mechanics and Engineering*, Vol. 194 Nos 18/20, pp. 2043-57.

Luo, H., Baum, J.D. and Löhner, R. (1994), "Edge-based finite-element scheme for the Euler equations", *AIAA*, Vol. 32 No. 6, pp. 1183-90.

Magnico, P. (2003), "Hydrodynamic and transport properties of packed beds in small tube-to-sphere diameter ratio: pore-scale simulation using an Eulerian and a Lagrangian approach", *Chemical Engineering Science*, Vol. 58, pp. 5005-24.

Malan, A.G. (2002), "Investigation into the continuum thermodynamic modelling of investment casting shell-mould drying", PhD thesis, University of Wales, Swansea.

Malan, A.G., Lewis, R.W. and Nithiarasu, P. (2002), "An improved unsteady, unstructured, artificial compressibility, finite volume scheme for viscous incompressible flows: Part I. Theory and implementation", *International Journal for Numerical Methods in Engineering*, Vol. 54 No. 5, pp. 695-714.

Massarotti, N., Nithiarasu, P. and Zienkiewicz, O.C. (2001), "Natural convection in porous medium – fluid interface problems. The finite element analysis by using the CBS procedure", *International Journal of Numerical Methods for Heat and Fluid Flow*, Vol. 11 No. 5, pp. 473-90.

Mavriplis, D.J. (1990), "Accurate multigrid solution of the Euler equations on unstructured and adaptive meshes", *AIAA Journal*, Vol. 28 No. 2, pp. 213-21.

Morris, J.P., Zhu, Y. and Fox, P.J. (1999), "Parallel simulations of pore-scale flow through porous media", *Computers and Geotechnics*, Vol. 25, pp. 227-46.

Niessen, H.F. and Stöcker, B. (1997), *Data Sets of SANA Experiment: 1994-1996*, JUEL-3409, Forschungszentrum Jülich, Jülich.

Nithiarasu, P. (2003), "An efficient artificial compressibility (ac) scheme based on the characteristic based split (cbs) method for incompressible flow", *International Journal for Numerical Methods in Engineering*, Vol. 56 No. 13, pp. 1815-45.

Nithiarasu, P., Seetharamu, K.N. and Sundararajan, T. (1996), "Double-diffusive natural convection in an enclosure filled with fluid-saturated porous medium: a generalized non-Darcy approach", *Numerical Heat Transfer Part A – Applications*, Vol. 30 No. 4, pp. 413-26.

Nithiarasu, P., Seetharamu, K.N. and Sundararajan, T. (1999), "Numerical investigation of boyancy-driven flow in a fluid-saturated non-Darcian porous medium", *International Journal for Heat and Mass Transfer*, Vol. 42, pp. 1205-15.

Pan, C., Hilpert, M. and Miller, C.T. (2001), "Pore-scale modelling of saturated permeabilities in random sphere packings", *Physical Review. E, Statistical, Nonlinear, and Soft Matter Physics*, Vol. 64, p. 066702.

Poulikakos, D. and Bejan, A. (1985), "The departure of Darcy flow in natural convection in a vertical porous layer", *Physics of Fluids*, Vol. 28 No. 12, pp. 3477-84.

Prasad, V., Lauriat, G. and Kladias, N. (1992), "Non-Darcy natural convection in a vertical porous cavity", *Heat and Mass Transfer in Porous Media*, Elsevier, Oxford, pp. 293-314.

Radestock, J. and Jeschar, R. (1971), "Theoretische untersuchung der gegenseitigen beeinflussung von temperatur-und strömungsfeldern in schüttungen", *Chemie Ingenieur Technik*, Vol. 43 No. 24, pp. 1304-10.

Sørensen, K.A., Hassan, O., Morgan, K. and Weatherill, N.P. (2002), "Agglomerated multigrid on hybrid unstructured meshes for compressible flow", *International Journal for Numerical Methods in Fluids*, Vol. 40 Nos 3/4, pp. 593-603.

Vafai, K. and Tien, C.L. (1981), "Boundary and inertia effects on flow and heat transfer in porous media", *International Journal for Heat and Mass Transfer*, Vol. 24, pp. 195-203.

Vafai, K., Alkire, R.L. and Tien, C.L. (1985), "An experimental investigation of heat transfer in variable porosity media", *ASME Journal of Heat Transfer*, Vol. 107, pp. 642-7.

Vahdati, M., Morgan, K., Peraire, J. and Hassan, O. (1989), "A cell-vertex upwind unstructured grid solution procedure for high-speed compressible viscous flow", *Proceedings of the International Conference on Hypersonic Aerodynamics, Royal Aeronautical Society, London*, pp. 12.1-12.22.

van Staden, M.P., Janse van Rensburg, C. and Viljoen, C.F. (2004), "CFD modelling of high-temperature reactors", *Proceedings of the 4th South African Conference on Applied Mechanics, Johannesburg*.

Verkerk, E.C. (2000), "Dynamics of pebble-bed nuclear reactor in the direct Brayton cycle", PhD thesis, Delft University of Technology, Delft.

Whitaker, S. (1967), "Diffusion and dispersion in porous media", *American Institute of Chemical Engineers Journal*, Vol. 13, pp. 420-7.

Zehner, P. and Schlünder, E.U. (1970), "Wärmeleitfähigkeit von Schüttungen bei mäBigen Temperaturen", *Chemie Ingenieur Technik*, Vol. 42 No. 14, pp. 933-41.

Zienkiewicz, O.C. and Taylor, R.L. (2000), *The Finite Element Method: Volume 3 – Fluid Dynamics*, 5th ed., Butterworth-Heinemann, Oxford.

Corresponding author
A.G. Malan can be contacted at: amalan@csir.co.za